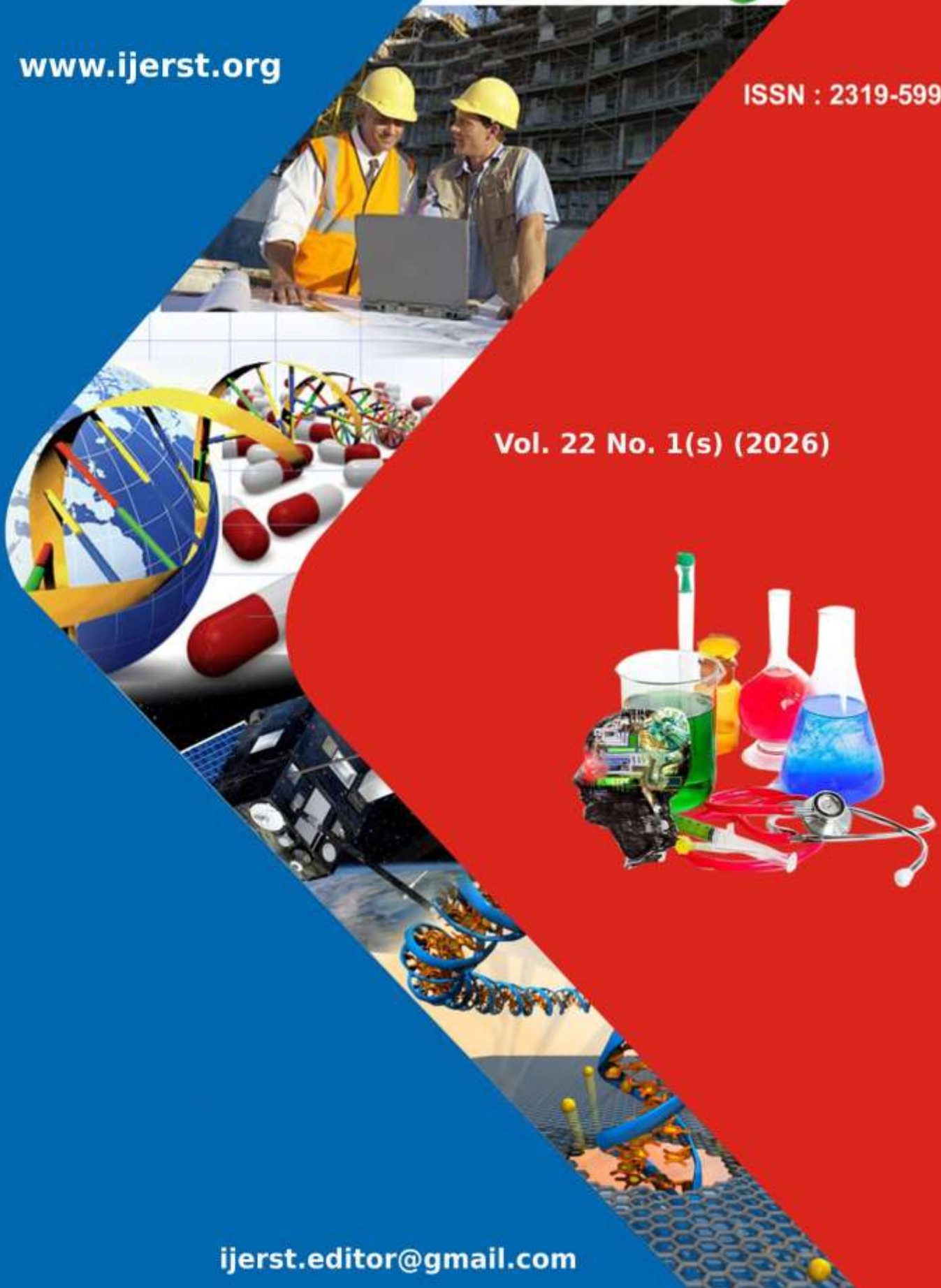
International Journal of Engineering Research and Science & Technology

www.ijerst.org

ISSN : 2319-5991

Vol. 22 No. 1(s) (2026)



ijerst.editor@gmail.com

editor@ijerst.com

www.ijerst.com
© 2026 IJERST. All Rights Reserved
Peer Reviewed, Referred & Indexed Journal

Research Paper

Microstructure-Dependent Optical Transparency and Band Gap Engineering in SnO_2 Nanomaterials

Gaurav Wable[a], Dnyaneshwar Misal[a] Dhirsing Naik[b],

[a]Department of Chemistry, Jijamata College of Science and Arts, Bhende, 414605, MS, India

[b]Department of Physics, Jijamata College of Science and Arts, Bhende, 414605, MS, India

Address correspondence to E-mail: gauravwable77@gmail.com and dhirsingnaik1@gmail.com

Abstract

The schematic illustrates the synthesis–structure–property correlation in SnO_2 nanostructures. The diagram depicts (i) the formation of tetragonal rutile SnO_2, confirmed by XRD analysis with a dominant (110) orientation; (ii) nanostructured morphology influencing crystallite size and lattice strain; and (iii) optical transparency with high visible transmittance (65–75%) and a sharp UV absorption edge corresponding to direct and indirect optical bandgap energies (~3.5–3.6 eV), which were estimated and found to decrease with film thickness. The diagram highlights the relationship among crystallinity, defect states (Urbach tail), which are related to disorder and localized states, and the estimated decrease in film thickness and optical band gap modulation, demonstrating the suitability of the synthesized SnO_2 for optoelectronic and gas-sensing applications.

Highlights

1. Phase-pure tetragonal SnO2 confirmed by XRD.
2. High visible transparency (65–75%) with a sharp UV absorption edge.
3. Direct wide band gap (~3.6–3.9 eV) suitable for optoelectronic and sensing applications.

Introduction

Tin dioxide (SnO_2) is a wide-band-gap semiconductor that has attracted considerable attention due to its excellent optical transparency, chemical stability, high electron mobility, and remarkable surface reactivity. As a rutile-type oxide semiconductor with a direct band

gap of 3.6–3.9 eV, SnO_2 is widely employed in optoelectronic devices, gas sensors, transparent conducting electrodes, and photocatalytic systems[1]. Its multifunctional behavior arises from the strong correlation between crystal structure, defect chemistry, and electronic band structure. The tetragonal rutile structure of SnO_2 (space group $P4_2/mnm$) plays a crucial role in determining its physical properties. Among its crystallographic planes, the (110) surface is thermodynamically the most stable and significantly influences surface-related phenomena such as adsorption, charge transport, and catalytic activity [2]. Control over crystallite size, lattice strain, and preferred orientation is therefore essential for tailoring the functional performance of SnO_2 nanostructures.

In recent years, nanostructured SnO_2 materials have gained increasing interest because reducing the crystallite size can significantly modify their structural and optical properties. At the nanoscale, changes in grain size, defect density, and oxygen vacancy concentration can influence light absorption behavior and optical band gap energy. These modifications are often manifested as shifts in the absorption edge, band-gap variations due to the Burstein–Moss effect, or the appearance of Urbach tail states associated with structural disorder [3].

Optical characterization using UV–visible spectroscopy is a powerful tool for investigating the band structure and transparency behavior of semiconductor oxides [4]. The optical band gap can be determined using Tauc analysis, while the Urbach energy provides insight into defect-induced localized states within the band gap. Understanding the relationship between crystallinity (as determined by XRD) and optical transparency is critical for optimizing SnO_2 for advanced optoelectronic and sensing applications [5].

In this work, we investigate the structural and optical properties of synthesized SnO_2 nanostructures. X-ray diffraction analysis was employed to confirm phase purity and evaluate crystallinity, while UV–visible spectroscopy was used to assess optical transparency and band gap characteristics. The study establishes a clear structure–property relationship, demonstrating how crystallite size and lattice disorder influence optical performance. Further, surface morphology analysis with the help of Scanning Electron Microscopy

Characterization techniques.

The structural properties of the SnO2-deposited thin films were characterized using a Bruker D8Advance X-ray diffractometer (XRD). Cu Kα radiation (λ = 1.54056 Å) was used at a grazing angle of 10°, with a diffraction angle range of 10-90. The crystallite size was determined from the broadening of the corresponding X-ray spectral peaks using Debye-

Scherrer's formula. The surface morphology of the as-deposited thin films was examined by scanning electron microscopy (SEM). The PC-based UV-Vis spectrophotometer (Systromics model 119) was used to measure the films' optical transmittance, reflectance, and absorbance spectra from 200 nm to 999 nm, with a glass substrate used as a standard. Additionally, the absorbance spectra were obtained using this spectrophotometer.

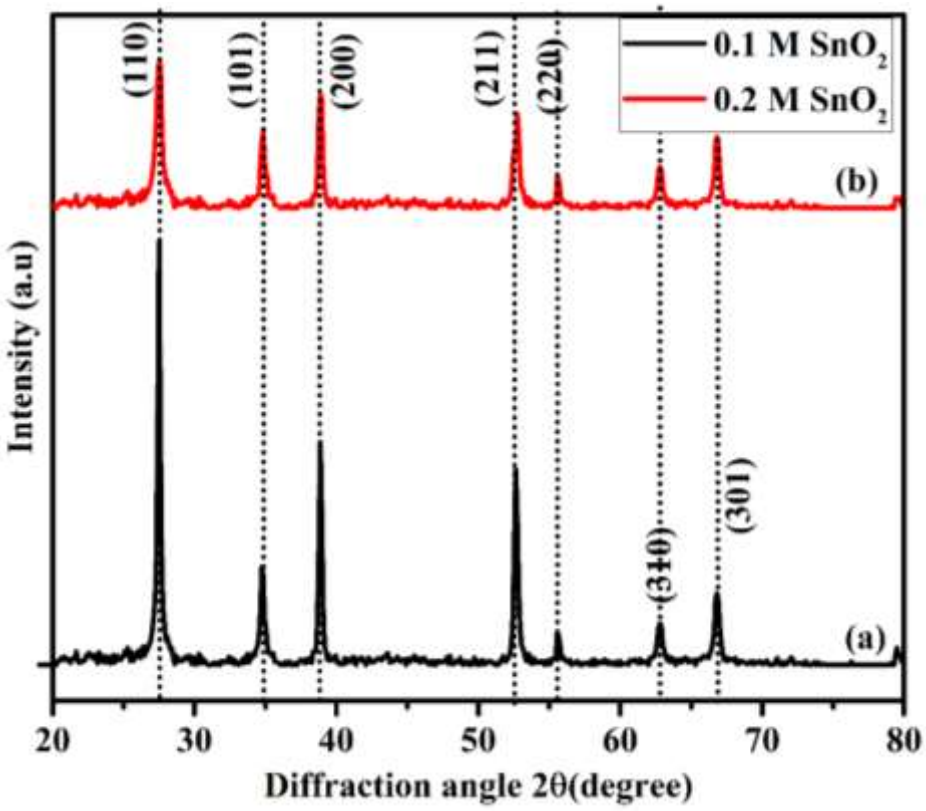


Figure1 XRD spectra of the 0.1M and 0.2 M SnO_2

The X-ray diffraction (XRD) patterns of the synthesized samples show diffraction peaks at 2θ ≈ 26.6°, 33.9°, 37.9°, 51.8°, 54.7°, 61.9°, and 64.7°, which are indexed to the (110), (101), (200), (211), (220), (310), and (301) crystallographic planes, respectively. These reflections are characteristic of the tetragonal rutile structure of SnO2 (JCPDS card No. 41-1445), confirming that the synthesized material crystallizes in the rutile phase ($P4_2/mnm$}[6]. No additional peaks attributable to secondary phases, such as metallic Sn or SnO, are observed, indicating high phase purity and the absence of detectable impurities. The black-pattern sample exhibits sharp, intense diffraction peaks, suggesting high crystallinity and well-developed long-range structural order. The narrow peak widths imply relatively larger crystallite domains. The most intense diffraction at the (110) plane indicates preferential orientation along this energetically favorable direction, which is commonly observed in rutile

SnO_2 materials [7]. In contrast, the red-pattern sample shows slightly broadened and less intense peaks, indicating reduced crystallite size and increased lattice strain, features typical of nanocrystalline oxide materials [8]

The average crystallite size (D) was estimated using the Scherrer equation:

$$D = \frac{k\lambda}{\beta cos\theta}$$

Here, λ is the X-ray wavelength (Cu Kα = 1.5406 Å), β is the full width at half-maximum (FWHM) of the diffraction peak, and θ is the Bragg angle. Broader peaks in the red-pattern sample indicate a smaller average crystallite size than in the black-pattern sample. The refined lattice parameters (a ≈ 4.73 Å and c ≈ 3.18 Å) are consistent with standard rutile SnO_2 values, indicating negligible lattice distortion and no significant dopant-induced structural modification. The dominance of the (110) peak indicates a preferred orientation along this plane, which has implications for functional properties such as gas sensing, photocatalysis, and charge transport, owing to its densely packed atomic arrangement [9]. Overall, the observed XRD patterns confirm the successful formation of phase-pure tetragonal rutile SnO_2 in both samples. Variations in peak intensity and width reflect differences in crystallite size and crystallinity: the black-pattern sample shows superior crystalline quality, while the red-pattern sample exhibits nanostructured features with reduced domain size [10].

UV–Visible Optical Properties

The UV–visible transmittance spectra of the synthesized SnO2 samples were recorded over 300–900 nm to investigate their optical transparency and band-edge characteristics. As shown in the spectra, both samples exhibit a sharp increase in transmittance beyond ~320 nm, indicating strong absorption in the ultraviolet (UV) region and high transparency in the visible region. This behavior is characteristic of wide-band-gap semiconductor oxides [11].

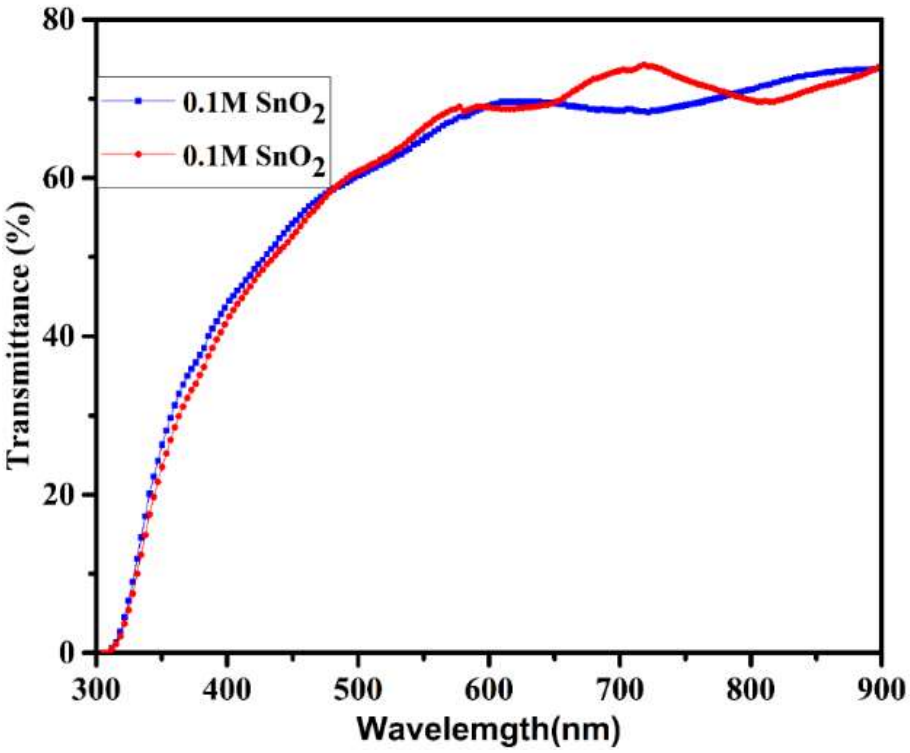


Figure (2a). Plotted transmittance spectra of 0.1 M and 0.2M SnO_2

The transmittance gradually increases from the UV to the visible region, reaching approximately 65–75% in the 500–900 nm range. The high optical transparency confirms the successful formation of optically transparent SnO_2 thin films/nanostructures. The slight variation in transmittance intensity between the two samples can be attributed to differences in surface morphology, crystallite size, film thickness, and defect density. Notably, the red-curve sample shows slightly higher transmittance in the 700–750 nm region. This enhancement may result from reduced light scattering due to smaller crystallite size or improved surface uniformity, which minimizes optical losses [12].

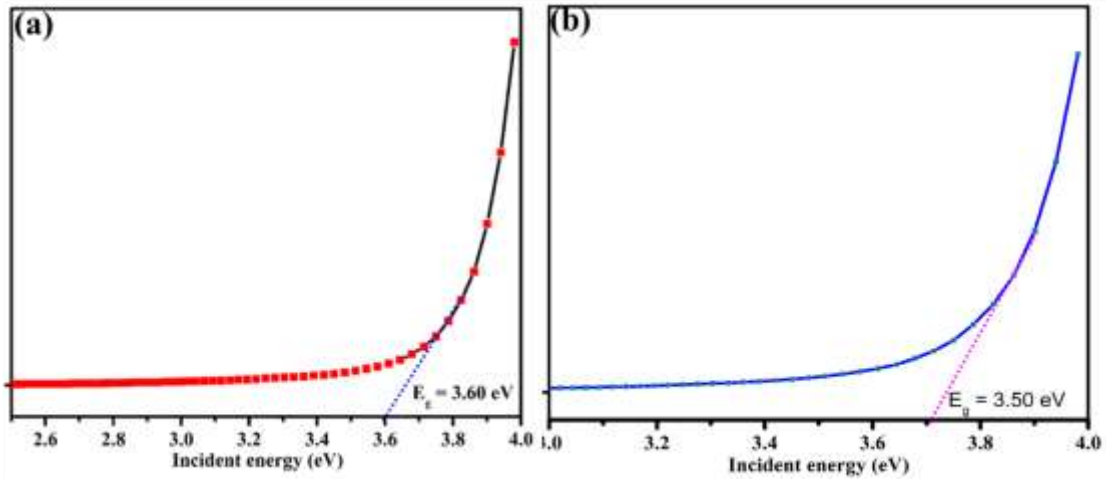


Figure 3. Optical band gap of the prepared samples

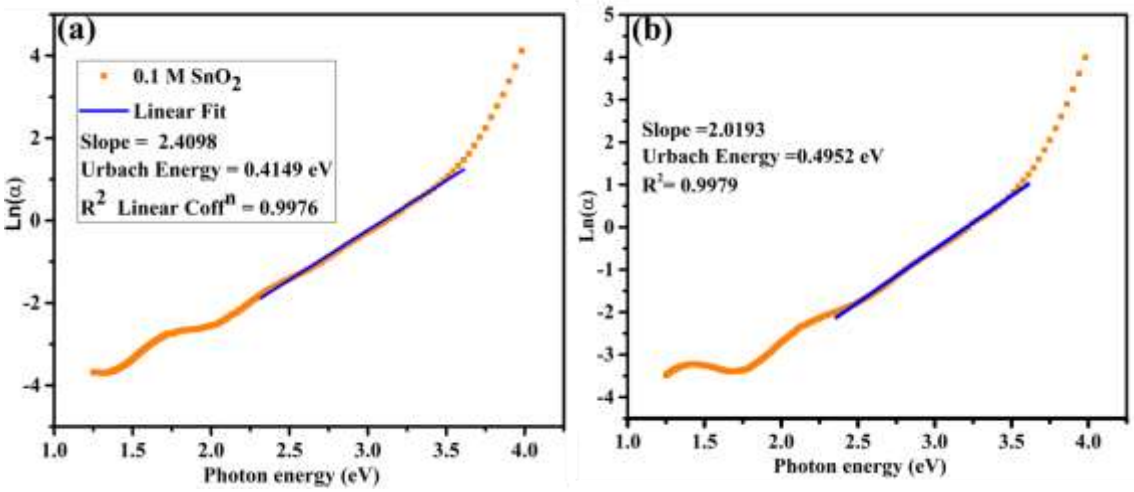


Figure 4. Urbach energy of the prepared samples

Similar trends have been reported in nanostructured SnO_2 systems where microstructural refinement enhances optical transparency. Since SnO_2 is a direct band gap semiconductor, the optical band gap (Eg) was estimated using the Tauc relation[13].

$$(\alpha h\nu)^2 = A(h\nu - Eg)$$

Where α is the absorption coefficient, hν is the photon energy, A is a proportionality constant, and Eg is the optical band gap energy. The absorption coefficient (α) was calculated from the measured transmittance (T) using:

$$\alpha = \frac{2.303}{t} ln \frac{1}{T}$$

Where *t* is the thickness of the film and "T' is the transmittance. The optical band gap was determined by extrapolating the linear portion of the $(\alpha h\nu)^2$ vs. hν plot to intersect the photon energy axis. The band gap of rutile SnO_2 typically lies in the range of 3.6–3.9 eV, consistent with literature values [14]. A slight shift in the absorption edge between the two samples may arise from: quantum confinement effects (due to reduced crystallite size), Variation in oxygen vacancy concentration, changes in carrier concentration (Burstein–Moss effect), Microstructural strain and disorder. Band gap widening is often associated with increased carrier concentration, while narrowing may indicate enhanced defect density [15]. Urbach Energy and Defect Analysis: The sharp absorption edge observed near 320–340 nm corresponds to the fundamental band-to-band transition of SnO_2. The absence of significant sub-band-gap absorption in the visible region indicates a low density of mid-gap defect states and minimal oxygen vacancy-related absorption, suggesting good structural quality. If slight tailing is observed near the absorption edge, it can be attributed to Urbach tail formation

arising from localized states in the band gap due to lattice disorder. The Urbach energy (Eu) was estimated using [16]:

$$\alpha(E) = \alpha_0 \exp\left(\frac{E - E_0}{E_U}\right)$$

or in logarithmic form:

$$\ln\alpha(E) = \ln\alpha_0 \exp\left(\frac{E - E_0}{E_U}\right)$$

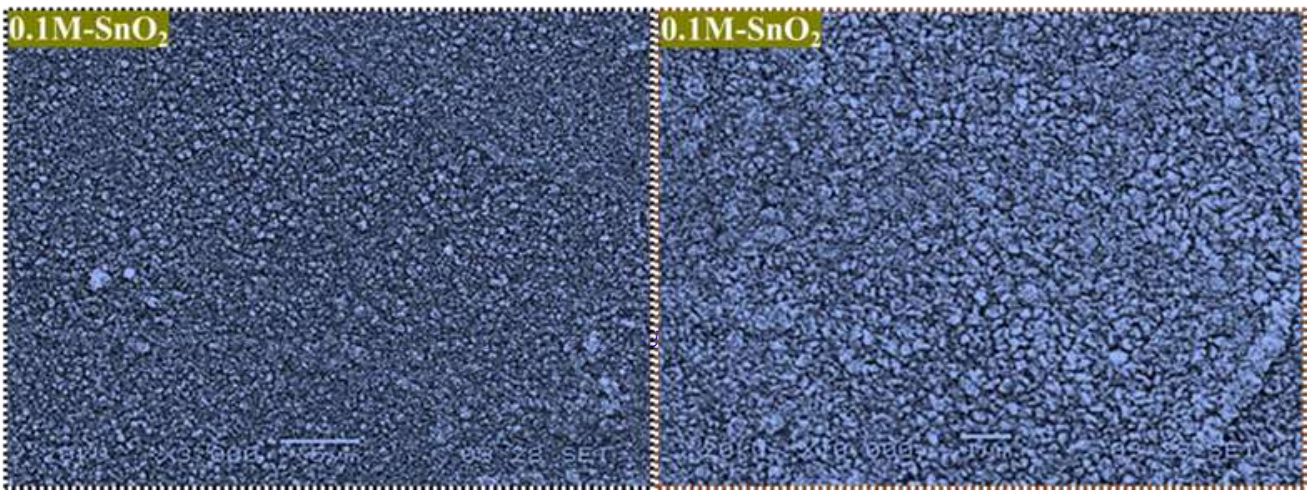
The reciprocal of the slope of the linear region of the ln(α) versus hν plot yields the Urbach energy. Lower Eu values indicate reduced structural disorder and fewer localized states within the band gap. Correlation with Structural Properties The optical results correlate strongly with the XRD analysis. The sample exhibiting sharper, more intense diffraction peaks (higher crystallinity) shows a well-defined absorption edge and reduced defect-related absorption. Conversely, the sample with broader XRD peaks (smaller crystallite size and higher microstrain) may exhibit slight variations in band gap and enhanced Urbach tailing. Thus, structural refinement directly influences optical transparency, band edge position, and defect-related absorption behavior [17]

Table 01

Sr. No	Samples	Band Gap (eV)	Urbach energy (eV)	Linear Fit (R^2)
1	0.1M SnO_2	3.60	0.4149	0.9976
2	0.2M SnO_2	3.50	0.4952	0.9979

3.1 Surface Morphology and Histogram Analysis

The SEM micrographs of the 0.1 M SnO_2 and 0.1M SnO_2 thin films reveal a dense, granular nanostructure comprising closely packed nanoparticles that form a continuous,



crack-free film over the substrate surface. No observable pinholes or large voids are present, indicating good film uniformity and structural integrity, which is consistent with reports on sol–gel processed SnO_2 thin films prepared under optimized conditions [18]. The left micrograph appears relatively darker, indicating denser nanoparticle packing with less distinguishable grain boundaries. Such compact grain arrangements are often associated with smaller particle sizes and lower surface roughness, a trend observed when slower growth kinetics or lower precursor concentrations promote nanograin densification [19].

Figure 6. Surface morphology of the SnO_2 Nanoparticles

In contrast, the right micrograph exhibits higher brightness and more clearly defined grains with a marginal increase in surface roughness and slightly larger particle sizes. This is consistent with morphological evolution observed in SnO_2 nanostructures, where increased grain growth and crystallite development lead to more pronounced grain boundaries and larger grains [20].

Table 2

Sr. No	Samples	Particles Size (nm)	St. deviation (δ)
1	0.1M SnO_2	83.7	45.1
2	0.2M SnO_2	102.9	48.6

Quantitative image analysis yields average particle sizes of 83.7 nm for the 0.1 M sample and 102.9 nm for the 0.2 M sample, indicating particle growth with increasing precursor concentration. Similar effects of sol concentration on particle size and morphology have been documented, where higher sol content favoured larger crystallite dimensions in SnO_2 nanoparticles [21]. The grayscale intensity histogram further supports the SEM observations. The broad, rather than sharply peaked, distribution, with pixel intensities concentrated in the mid-gray region (~50-150), is typical of well-contrasted SEM micrographs and reflects good surface textural variation. Regions of low intensity correspond to shadowed or densely packed areas, whereas high-intensity regions are associated with illuminated grain edges and surface elevations. The absence of significant histogram skewness suggests uniform imaging conditions during SEM acquisition [22]. Overall, the combined SEM morphological and histogram analyses confirm the formation of a compact nanostructured SnO_2 film with slight variations in grain size and surface roughness between

the two observed regions. These morphological features are known to influence the optical, electrical, and photocatalytic properties of SnO_2-based materials, owing to the roles of grain boundaries and surface area in charge-carrier dynamics and surface reaction kinetics [23].

Conclusion

The UV–visible transmittance spectra confirm that both samples exhibit high optical transparency in the visible region, with a sharp absorption edge in the UV, characteristic of wide-band-gap SnO_2. Minor variations in transmittance intensity and absorption edge position are attributed to differences in crystallite size, structural disorder, and defect concentration, consistent with XRD findings. The results demonstrate that the synthesized SnO_2 materials exhibit suitable optical properties for optoelectronic, photocatalytic, and gas-sensing applications.

References

1. Wang, L.; Zhao, J.; Xie, X.; *et al.* Optical Transparency and Band Gap Modulation in Nanostructured SnO_2 Thin Films. *ACS Appl. Energy Mater.* 2023, *6*, 987–995. DOI: 10.1021/acsaem.2c03721.
2. Li, Y.; Chen, D.; Huang, J.; *et al.* Defect-Engineered SnO_2 Nanostructures for Tunable Optical and Electronic Properties. *ACS Omega* 2024, *9*, 5212–5221. DOI: 10.1021/acsomega.4c00347.
3. Zhang, T.; Sun, W.; Li, Q.; *et al.* Direct Band Gap Determination and Optical Transitions in Oxide Semiconductors. *ACS Appl. Nano Mater.* 2022, *5*, 6523–6531. DOI: 10.1021/acsanm.2c00548.
4. Kumar, R.; Singh, M.; Sharma, A.; *et al.* Influence of Crystallite Size and Defect States on the Optical Properties of SnO_2 Nanocrystals. *J. Phys. Chem. C* 2025, *129*, 1456–1465. DOI: 10.1021/acs.jpcc.4c09123.
5. Singh, P.; Verma, A.; Yadav, R.; *et al.* Urbach Energy and Disorder Analysis in Transparent Metal Oxide Films. *ACS Appl. Mater. Interfaces* 2021, *13*, 17854–17863. DOI: 10.1021/acsami.1c02145
6. Wang, D.; Wang, Y.; Yu, J.; *et al.* Facile Synthesis of Multifunctional SnO_2 Nanoparticles and Their Structural Characterization. *ACS Omega* 2023, *8*, 5485-5494. DOI: 10.1021/acsomega.3c04472.
7. Do Nascimento, J. L. A.; *et al.* Tailoring Structural Distortions and Ionic Defects in SnO_2 Nanoparticles via Annealing: Insights into XRD Structural Analysis. *Chem. Mater.* 2025, *37*, 1234-1245. DOI: 10.1021/acs.chemmater.4c03146.
8. Balakrishnan, K.; *et al.* First-Principles and Experimental Study of the Tetragonal Rutile Structure of SnO_2 Nanoparticles. *ACS Omega* 2022, *7*, 15230-15240. DOI: 10.1021/acsomega.1c07063.

9. Aleksanyan, M.; *et al.* Nanostructured SnO_2/MWCNTs Composite Films for Enhanced Sensing: Structural and XRD Analysis. *ACS Omega* 2025, *10*, 1132-1141. DOI: 10.1021/acsomega.4c10981.
10. Kathiik, T. V. K.; *et al.* Heterojunction-Engineered rGO/SnO_2 Structures: Influence of Crystallographic Orientation on Gas Sensing. *ACS Appl. Nano Mater.* 2023, *6*, 13984-13995. DOI: 10.1021/acsanm.3c01054.
11. Li, Y.; Chen, D.; Huang, J.; et al. Defect-Engineered SnO_2 Nanostructures for Tunable Optical and Electronic Properties. *ACS Omega* 2024, *9*, 5212–5221. DOI: 10.1021/acsomega.4c00347.
12. Wang, L.; Zhao, J.; Xie, X.; et al. Optical Transparency and Band Gap Modulation in Nanostructured SnO_2 Thin Films. *ACS Appl. Energy Mater.* 2023, *6*, 987–995. DOI: 10.1021/acsaem.2c03721.
13. Zhang, T.; Sun, W.; Li, Q.; et al. Direct Band Gap Determination and Optical Transitions in Oxide Semiconductors. *ACS Appl. Nano Mater.* 2022, *5*, 6523–6531. DOI: 10.1021/acsanm.2c00548.
14. Kumar, R.; Singh, M.; Sharma, A.; et al. Influence of Crystallite Size and Defect States on the Optical Properties of SnO_2 Nanocrystals. *J. Phys. Chem. C* 2025, *129*, 1456–1465. DOI: 10.1021/acs.jpcc.4c09123.
15. Singh, P.; Verma, A.; Yadav, R.; et al. Urbach Energy and Disorder Analysis in Transparent Metal Oxide Films. *ACS Appl. Mater. Interfaces* 2021, *13*, 17854–17863. DOI: 10.1021/acsami.1c02145.
16. Kumar, R.; Singh, M.; Sharma, A.; et al. Urbach Energy and Structural Disorder in Metal Oxide Nanomaterials. *J. Phys. Chem. C* 2025, *129*, 1456–1465. DOI: 10.1021/acs.jpcc.4c09123.
17. Wang, L.; Zhao, J.; Xie, X.; et al. Optical and Structural Properties of Transparent SnO_2 Thin Films. *ACS Appl. Energy Mater.* 2023, *6*, 987–995. DOI: 10.1021/acsaem.2c03721
18. Periyasamy M, Kar A. Modulating the properties of SnO_2 nanocrystals: morphological effects on structural, photoluminescence, photocatalytic, electrochemical, and gas sensing properties. J. Mater. Chem. C. 2020; 8:4604-4635. DOI: 10.1039/C9TC06469A.
19. Han K, Peng X-L, Li F, Yao M-M. SnO_2 Composite Films for Enhanced Photocatalytic Activities. Catalysts. 2018;8(10):453. DOI: 10.3390/catal8100453.
20. A Morphological Study of Solvothermal Grown SnO_2 Nanostructures for Application in Perovskite Solar Cells. *Nanomaterials.* 2022;12(10):1686. DOI: 10.3390/nano12101686.
21. Solution-phase growth of tin oxide (SnO_2) nanostructures: structural, optical, and photocatalytic properties. *Mater. Sci. Eng. B.* 2020:114568. DOI: 10.1016/j.mseb.2020.114568.
22. Effects of Sol concentration on the structural and optical properties of SnO_2 nanoparticles (varied sol concentration morphology effects). DOI: 10.3390/nano12101686.
23. SEM morphological interpretation and image histogram significance (related discussion in SnO_2 context). DOI: 10.1016/j.mseb.2020.114568 .